

Choosing the Optimal Power Coils Using Open-Source k-Oriented Design Automation

Chaebin Kim, *Member, IEEE*, Edward Nichols, *Student Member, IEEE*, and Brian N. Kim , *Member, IEEE*

Abstract—Wireless power coils have found important use in implantable medical devices for safe and reliable wireless power transfer. Designing coils for each specific application is a complex process with many interdependent design variables; determining the most optimal design parameters for each pair is challenging and time-consuming. In this paper, we develop an automated design method for planar square-spiral coils that generates the idealized design parameters for maximum power transfer efficiency according to the input design requirements. Computational complexity is first reduced by isolating the inductive coupling coefficient, k , from other design parameters. A simplified but accurate equivalent circuit model is then developed, where skin effect, proximity effect, and parasitic capacitive coupling are iteratively considered. The proposed method is implemented in an open-source software which accounts for the input fabrication limitations and application specific requirements. The accuracy of the estimated power transfer efficiency is validated via finite element method simulation. Using the presented approach, the coil design process is fully automated and can be done in few minutes.

Index Terms—Biomedical implantable devices, design automation, inductive-link coupling coefficient, open-source, square-spiral, wireless power transfer.

I. INTRODUCTION

WIRELESS power transfer allows implantable medical devices to operate without a persisting risk of infection or periodic surgery for battery replacement. To implement wireless power transfer, various methods are developed using coils, antennas, or ultrasonic transducers. Wireless power transfer using near-field inductive-linked coils (Fig. 1a) is the standard method to deliver power to operate high-performance neural implants due to its superior power transfer efficiency (PTE) [1], [2]. In contrast, wireless power transfer by far-field antennas or ultrasonic transducers is more suitable for sending low power to an implant deep in a tissue [3]–[5].

Numerous scientific papers have proposed design methodology and shown analytic models for an inductive link [6]–[10]. However, designing the wireless power transfer system remains an analytically complex and time-consuming task because of

the large number of interdependent variables to account for. In addition, the standard tool for designing coils is finite element method (FEM) simulation software. To get accurate results from simulations, coil-design engineers are required to have knowledge in electromagnetics and have access to substantial computational resources. Hence, there is a need for a more practical design tool for researchers and engineers working to implement wireless power transfer in their implantable biomedical electronic systems.

This paper presents an efficient design automation method for wireless power coils, developed with an open-source application. Our program yields the optimal coil pair at maximum power efficiency according to the given design constraints. The coupling coefficient-oriented methodology is used as the basis of the design algorithm. Essentially, design parameters which are dependent upon the coupling-coefficient (k) are first optimized to achieve maximum k . Then, those design parameters which are relatively independent to k are optimized for maximum PTE. By splitting the optimization process into two consecutive steps, the computational complexity of the process is reduced by orders of magnitude. To identify k -dependent and k -independent parameters, the marginal impact to k is analyzed with respect to each design variable using FEM (Section II). The result show that k is dependent primarily upon the distance between the coils and the outer and inner diameters of the coils. Power coils for implantable biomedical devices share similar constraints in their separation distance and size, so values of k corresponding to a relevant and characteristic set of the k -dependent variables are obtained from FEM and saved as reference throughout the design processes. From the data, it is possible to identify the optimal outer and inner diameters which maximize k given a distance between the coils. For the rest of the design parameters, iteration starts over the parameters for each coil to achieve maximum PTE (Section III). To estimate PTE without running FEM at each iteration of the parameters, an equivalent circuit model for each coil is developed (Section IV). Calculated power transfer efficiency with respect to each design variable is validated by comparing the power transfer efficiency from a corresponding FEM as well as fabricated coils (Section V). Using the proposed design procedure and analytic model, this paper presents an open-source software that yields the coils with the highest PTE (Section VI). Our program allows designers to not only achieve maximum PTE but also study the relationship of the design parameters and constraints to PTE. The vision for future work and some concluding remarks are given in Section VII.

Manuscript received October 20, 2020; revised January 11, 2021; accepted February 1, 2021. Date of publication March 17, 2021; date of current version March 30, 2021. This work was supported by National Science Foundation under Grant #1745364. This article was approved by Associate Editor Yaoyao Jia. (*Corresponding author: Brian N. Kim.*)

The authors are with the Department of Electrical and Computer Engineering, University of Central Florida, Orlando, FL 32816 USA (e-mail: chae.b.kim@gmail.com; enichols25@knights.ucf.edu; brian.kim@ucf.edu).

Color versions of one or more figures in this article are available at <https://doi.org/10.1109/TBCAS.2021.3059934>.

Digital Object Identifier 10.1109/TBCAS.2021.3059934

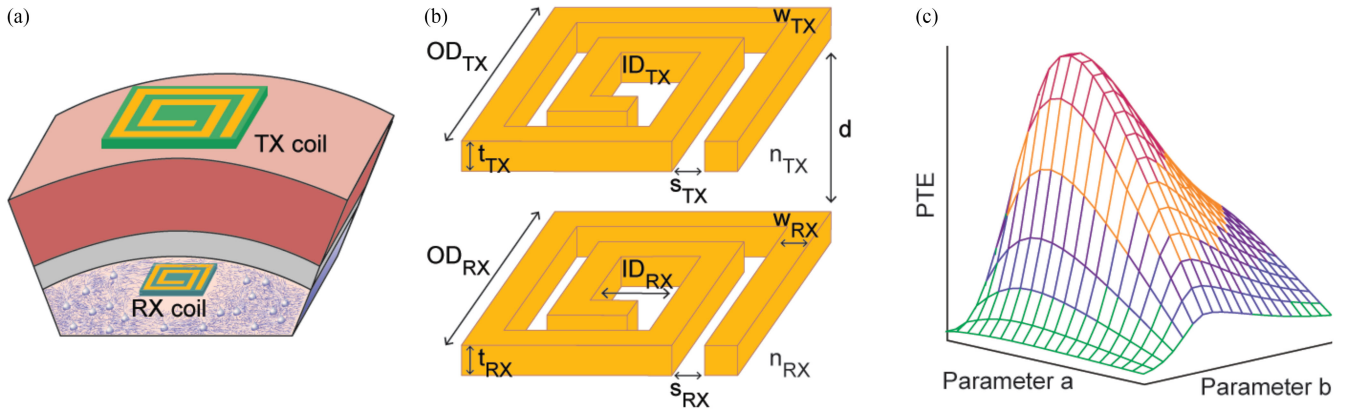


Fig. 1. Overview of this study. (a) The scope of this study is to design transmitting (TX) coil and receiving (RX) coil for implants. (b) Design parameters are defined as the distance between the coils (d), outer diameter (OD), inner diameter (ID), planar thickness (t), turn spacing (s), spiral width (w), and turn count (n) of each coil. (c) Power transfer efficiency (PTE) is maximized by optimizing the design parameters. Parameter a and b can be any set of design parameters listed above.

II. DECOUPLING k FROM CRITICAL DESIGN PARAMETERS

The coupling-coefficient, k , is the ratio of the magnetic flux through a coil to the magnetic flux through its counterpart. Since the voltage induced on a coil is proportional to the change in magnetic flux through the coil, the induced voltage across the receiver coil (RX) is proportional to the product of k and the change in magnetic flux at the transmission coil (TX). Because the transferred power is proportional to the square of the induced voltage, the power to the receiver coil is proportional to k^2 times the square of the change in magnetic flux of the transmitter coil. Ultimately, maximizing k achieves high PTE in wireless power transfer coil pair design [9] and therefore employ this objective is employed in the design methodology outlined in this paper.

We begin with determining the geometric shape of the coils. In this paper, the square spiral is selected because IC chips are typically rectangular, spirals have relatively good area efficiency, and planar geometry is compatible with lithography. Based upon our convenient geometry, the design parameters which are critical to PTE are the distance between the coils, their outer diameters, inner diameters, planar thickness, turn spacing, spiral width, and turn count (Fig. 1b). The relationships between PTE and the design parameters are nonlinear; optimization processes of the critical design parameters for maximum PTE are often heuristic [12], [13]. To simplify the design parameters. An example of a simplified optimization process is the design methodology for mm-sized RX coil and cm-sized TX coil pairs [6], [14], [15]. Each coil is separately optimized for maximum PTE because the magnetic field of the TX coil is constant regardless of the RX coil [16], [17]. This strategy is also applied to coil design in general for the parameters that are independent from k [8].

Here, the dependencies of k to design parameters are investigated via simulation to identify those parameters which are most decoupled from k . To narrow the vast field of possible configurations, the simulation effort centers and sweeps about sets of design parameters (and thus a range of k values) which are of current practical interest. For example, pairs of

coil models are generated based on design parameters where the distance between coils are relevant to neural implants (15 mm) (Section III). Two-port impedance parameters are obtained from the simulation result. As coupling coefficient is defined as the ratio of the mutual inductance to the geometric average of self-inductances, k is computed from the impedance parameters as $\frac{\text{Im}(Z_{TX-RX})}{\sqrt{\text{Im}(Z_{TX-TX})\text{Im}(Z_{RX-RX})}}$ [6].

To test the relative dependencies of each design parameter, the IDs and ODs of both RX (ID_{RX} : 4 mm, OD_{RX} : 5 mm) and TX coils (ID_{TX} : 10 mm, OD_{TX} : 50 mm) are fixed, to then vary each of the remaining design parameters (Fig. 2). When the metal thickness of the RX coil is varied from 1–10 μm , the average k value is 1.51×10^{-2} and the standard deviation is 0.02×10^{-2} for the entire range (Fig. 2a). The relative change in k from a change in thickness is negligible, and therefore, thickness can be treated as an independent parameter. The same observation applies to the turn spacing, spiral width, and number of turns for both RX and TX coils. The deviation in k for every TX coil with the thickness between 1–100 μm is 0.01×10^{-2} which is less than a percentage point (Fig. 2b). The turn spacing of the RX coil within 1–50 μm also shows a k of 1.50×10^{-2} with marginal deviations below the significant digit (Fig. 2c). When the turn spacing of TX coil is between 0.1–2 mm, the deviation in measured k is about two percent (Fig. 2d). RX coils with a spiral width between 9–100 μm also demonstrate below one percentage point in deviation (Fig. 2e). When the spiral width of the TX coil is between 0.7–10 mm, k deviates within two percent (Fig. 2f). Varying the turn count of either the RX coil or the TX coil results in a deviation of less than $\sim 5\%$ (Fig. 2g–h), which remains relatively tolerable.

Therefore, in the tested range of planar thickness, spiral width, turn spacing, and turn count, the k value deviates within tolerable margins and can be pragmatically neglected. Because these parameters are decoupled from k , the optimization of the parameters can be performed separately on TX and RX coils, which reduces the computational burden.

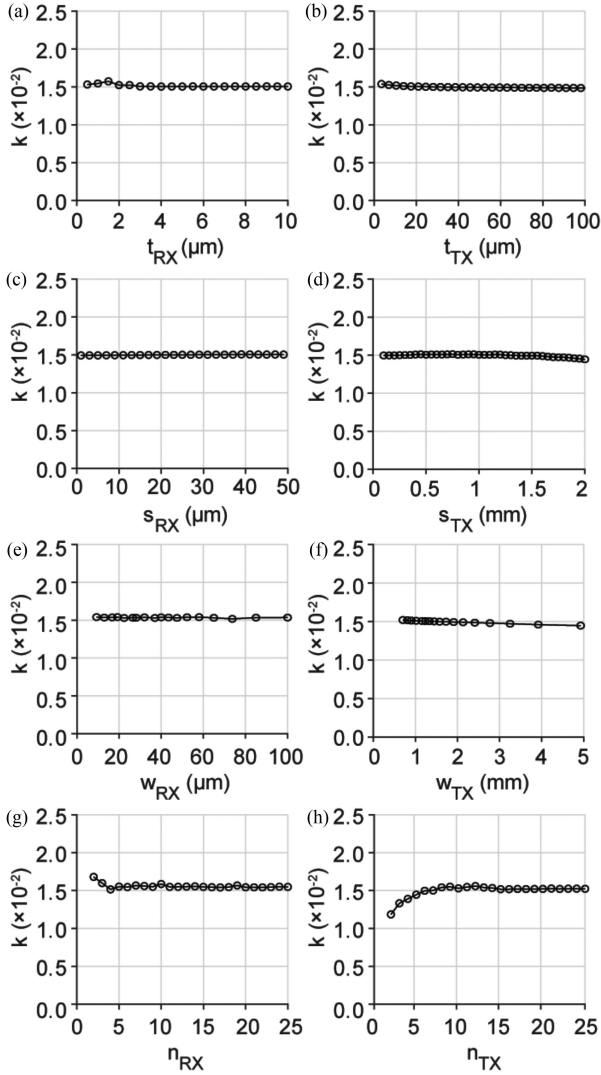


Fig. 2. Coupling coefficient (k) is extracted from as a function of geometrical design parameters: (a) planar thickness of RX coil, (b) planar thickness of TX coil, (c) turn spacing of RX coil, (d) turn spacing of TX coil, (e) spiral width of RX coil, (f) spiral width of TX coil, (g) number of turns in RX coil, and (h) number of turns in TX coil.

III. COIL DESIGN FLOW

Each biomedical implant's application has a set of intrinsic constraints including the minimum gap (d) between the parallel TX and RX coils and the maximum size of the implantable device and hence the RX coil (OD_{RX}). According to observations in Fig. 2, k is mainly a function of d , and the diameters of the RX and TX coils. To maximize the power efficiency, d is to be selected as the minimum value possible and OD_{RX} is to be selected as the maximum value. Because d and OD_{RX} is set by the application constraints, ID_{RX} , OD_{TX} , and ID_{TX} are the remaining parameters to be determined. The application-specific parameters, d and OD_{RX} , provide the basis for determining an upper boundary in the k value (max- k) for that application.

From d and OD_{RX} , it is possible to select from a range of ID_{RX} , OD_{TX} , and ID_{TX} values which render at least 95% of k 's maximum value. Multiple sets of ID_{RX} , OD_{TX} , and ID_{TX}

TABLE I
PARAMETERS FOR TX AND RX COILS

| Parameter | Symbol |
|---------------------------------|-----------|
| Distance between TX and RX coil | d |
| Outer diameter of RX coil | OD_{RX} |
| Outer diameter of TX coil | OD_{TX} |
| Inner diameter of RX coil | ID_{RX} |
| Inner diameter of TX coil | ID_{TX} |
| Planar thickness of RX coil | t_{RX} |
| Planar thickness of TX coil | t_{TX} |
| Turn spacing of RX coil | s_{RX} |
| Turn spacing of TX coil | s_{TX} |
| Spiral width of RX coil | w_{RX} |
| Spiral width of TX coil | w_{TX} |
| Turn count of RX coil | n_{RX} |
| Turn count of TX coil | n_{TX} |

TABLE II
DESIGN PARAMETERS INDEPENDENT TO K

| Parameter | Range | Deviation of k |
|-----------|---------------------------|------------------|
| t_{RX} | 1 – 10 μm | 1.3 % |
| t_{TX} | 1 – 100 μm | 0.8 % |
| s_{RX} | 1 – 50 μm | 0.3 % |
| s_{TX} | 0.1 – 2 mm | 1.6 % |
| w_{RX} | 20 – 200 μm | 0.8 % |
| w_{TX} | 900 – 10000 μm | 2.1 % |
| n_{RX} | 2 – 25 | 1.9 % |
| n_{TX} | 2 – 25 | 5.5 % |

The distance between the coils (d) is 15 mm, outer diameter of RX coil (OD_{RX}) is 5 mm, inner diameter of RX coil (ID_{RX}) is 4 mm, outer diameter of TX coil (OD_{TX}) is 50 mm, and inner diameter of TX coil (ID_{TX}) is 10 mm.

TABLE III
K-DEPENDENT DESIGN PARAMETERS

| Parameter [†] | Range |
|------------------------|---------------|
| OD_{RX} | 5 – 75 mm |
| OD_{TX} / OD_{RX} | 0.1 – 15 |
| ID_{RX} / OD_{RX} | 0.025 – 0.975 |
| ID_{TX} / OD_{TX} | 0.025 – 0.975 |

The distance between the coils (d) is 15 mm

TABLE IV
PARAMETERS VALUES FOR VALIDATION STUDY WITH FEM

| Parameter | Value of RX coil | Value of TX coil |
|----------------|-------------------|------------------|
| Outer diameter | 15 mm | 50 mm |
| Inner diameter | 11 mm | 10 mm |
| Thickness | 30 μm | 0.5 mm |
| Width | 600 μm | 2.4 mm |
| Turn count | 3 | 5 |
| Spacing | 100 μm | 2 mm |

$d = 15$ mm, $f = 13.56$ MHz

can result in above 95% of max- k . The designer can make any selections according to their application's specific tradeoffs. From FEM simulations, k values from every possible coil pair within a certain range (Table III) are measured in relation to d , OD_{RX} , ID_{RX} , OD_{TX} , and ID_{TX} (Fig. 3). The distance between the coils is set by the thickness of the tissue between the implant and the external power transmission device, the thickness of the packaging of the implant, and the thickness of the packaging of the external device. The thickness of packaging and the depth

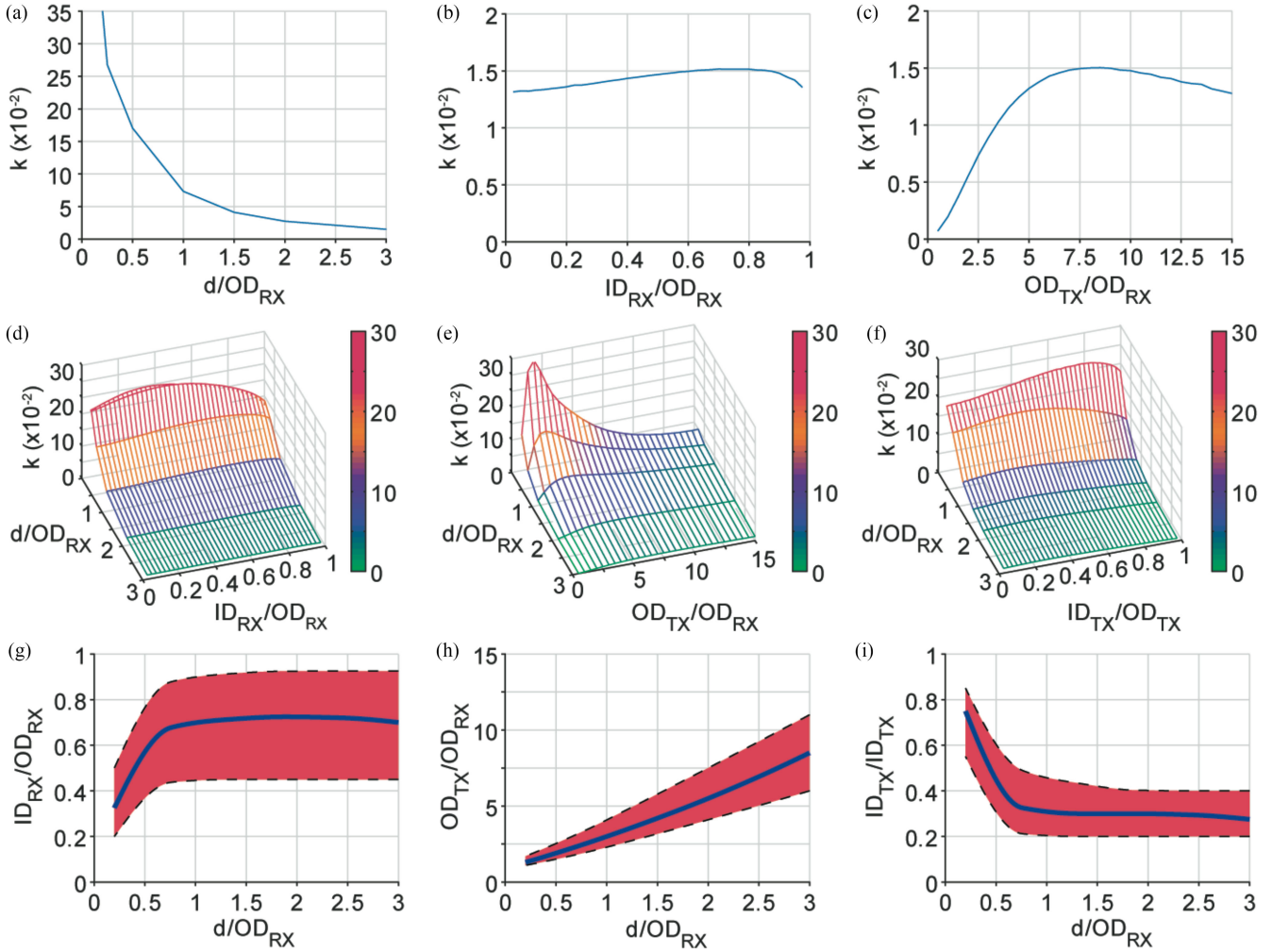


Fig. 3. Coupling coefficient as a function of the distance between the coils, outer diameters of the coils, and the inner diameters of the coils. Coupling coefficient is plotted with respect to (a) the outer diameter of RX coil, (b) the inner diameter of RX coil, (c) the outer diameter of TX coil, (d) the outer and inner diameter of RX coil, (e) the outer diameter of RX and TX coil, and (f) the outer diameter of RX coil and the inner diameter of TX coil. Optimum range of (g) the inner diameter of RX coil, (b) the outer diameter of TX coil, and (c) the inner diameter of TX coil to keep k within 95% of its maximum value are plotted for the different outer diameter of RX coil.

of implantation cannot be assumed as an exact value, but the distance between the coils may be chosen in conservative manner to tolerate the worst-case scenario.

The design flow chart is shown in Fig. 4. As the first step of this design flow, the set of d , OD_{RX} , ID_{RX} , OD_{TX} , and ID_{TX} is selected. Choosing a set of d , OD , and ID mostly defines k and thus enables optimization of power transfer efficiencies about the rest of the critical design parameters such as spiral width, planar thickness, turn spacing, and turn count. The accessible manufacturing capability sets the range of width, thickness, spacing, and turn counts which can be designed and fabricated. For example, in CMOS and PCB processes, the design rules have a minimum width and spacing, minimum incremental width and spacing, and a discrete set of metal thicknesses. A large RX coil size and a smaller gap between the coils, expressed as a low ratio between the two application-specific parameters, d and OD_{RX} , contribute the most to large k values (Fig. 3a–c). Fig. 3a–f shows the optimization process for k by varying k -dependent parameters. For a given d/OD_{RX} , the best k value is achieved by selecting an

ideal set of ID_{RX}/OD_{RX} , OD_{TX}/OD_{RX} , and selecting the rest of the parameters from the characteristic blue lines in Fig. 3g–i. If using the given ideal set imposes an unacceptable constraint or tradeoff in the design, which is foreseeable in some cases, choosing an acceptable set of ID_{RX}/OD_{RX} , OD_{TX}/OD_{RX} , and ID_{TX}/ID_{TX} from within the red area in Fig. 3g–i can also achieve near or above 95% of the max- k value. In general, ID_{RX} has little influence over the k value if the ID_{RX} value is not too close to OD_{RX} (Fig. 3g). The size of the ideal transmitter coil is mainly determined by the d/OD_{RX} ratio and the OD_{RX} size (Fig. 3h). If the size of the receiver coil and the gap is similar, and therefore, d/OD_{RX} is close to 1, the size of the transmitter coil must be ~ 2.5 times larger than OD_{RX} to achieve the highest k value.

After deciding ODs and IDs that maximize k , the next step is to iterate through remaining parameters to find the highest PTE. This portion can be fully automated. During the iterative search, an equivalent circuit of the coils is generated for each set of parameters. The circuit model is composed of the effective inductance, resistance, and capacitance of the coil; effective

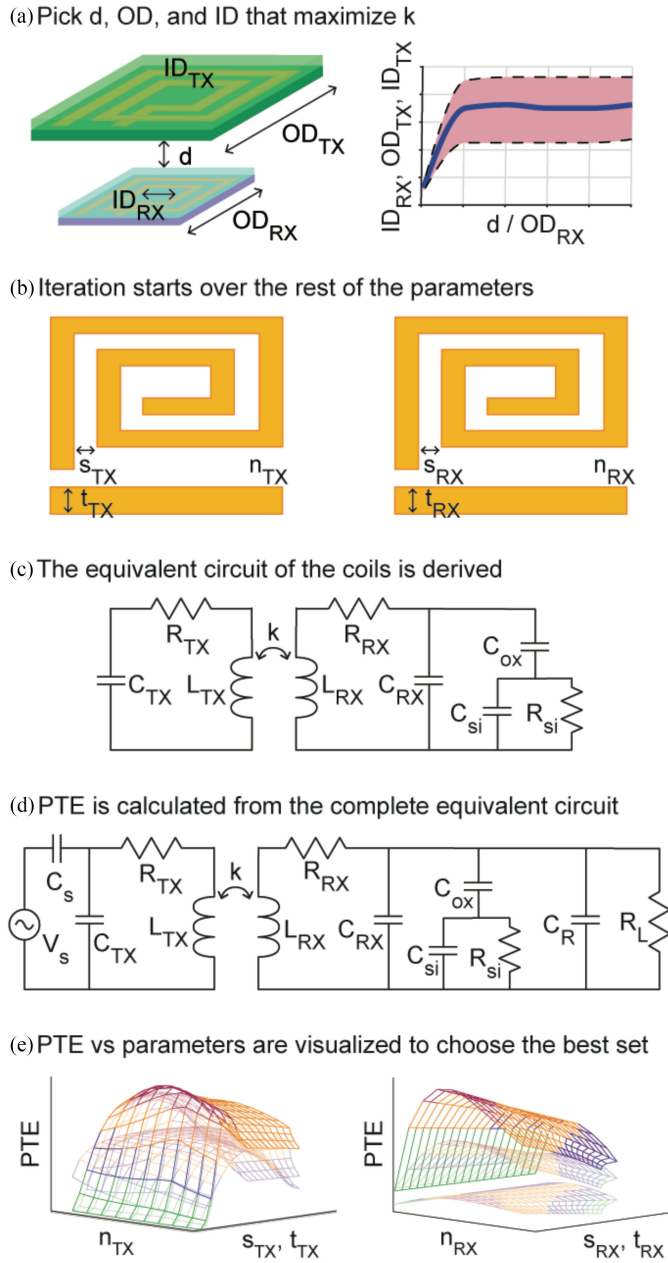


Fig. 4. Design flow chart. First, the distance between the coils, the outer diameter of the coils, and the inner diameter of the coils are determined to get the highest coupling coefficient. Then, width, spacing, thickness and turn count of each coil are iterated to find the optimum set of parameters that achieve a maximum power transfer efficiency. At each iteration, the power transfer efficiency is obtained from the equivalent circuit model.

inductance includes self-inductance of the segments in each turn; effective resistance considers skin and proximity effects; and the effective capacitance includes the distributed capacitance model. At this point, self-resonant frequency due to the inductance as well as the parasitic capacitance can be determined. In order to shift the resonant frequency to the operation frequency, tuning capacitor values for each coil can be calculated by considering parasitic capacitance values. Tuning capacitors are connected to each coil to ensure coil resonance in the operating frequency. The

optimal tuning capacitances for both TX and RX coils are calculated from their individual inductance values and self-resonating frequency. Solving the circuit using Kirchoff's laws an estimate for PTE from each set of design parameters is computed. After PTEs are calculated from all relevant combinations of parameters, the data can be visualized to provide insight on the coil design and choose the best set of parameters for implementation.

For example, in support of associated work for our lab, a brain machine interface (BMI) application is used as the primary design example. The thickness of the human skull varies from 3 mm to 8 mm [18]. Thickness of human dura mater can be up to 1.9 mm [19]. Thickness of human head skin can be up to 2 mm [20]. The thickness of implant and external device can also be a few mm, each. Hence, 15 mm is selected to represent a reasonable estimate of the worst-case-scenario- d for the application. The range of OD_{RX} swept from 5–15 mm encompasses the likely or possible sizes of neural implant devices. If we decide to use OD_{RX} of 15 mm, d/OD_{RX} is 1. Using Fig. 3h, OD_{TX}/OD_{RX} value between 2–4 will yield k within 95% of its maximum. Any OD_{TX} that satisfies between these values will be sufficient, but in this example, we choose 50 mm ($OD_{TX}/OD_{RX} = 3.33$). The outer diameters of both coils are now determined, and we proceed to determine the inner diameters. According to Fig. 3g, ID_{RX}/OD_{RX} of 0.45–0.9 should be used. We choose 10 mm which results in ID_{RX}/OD_{RX} of 0.67. For ID_{TX} , we use Fig. 3i, and choose 20 mm, which results in ID_{TX}/OD_{TX} of 0.4. With all diameter determined, the next step is to iterate through remaining parameters to calculate all possible PTEs. For this iteration, we input the fabrication constraints (minimum width = 0.1 mm, minimum spacing = 0.1 mm, and maximum thickness = 70 μ m). Each iteration determines a set of design parameters to test, and calculates the PTE. In this example, the highest PTE from all iterations is 83%. And the set of design parameters that results in the highest PTE is listed: $w_{RX} = 1.2$ mm, $w_{TX} = 593$ μ m, $t_{RX} = 56$ μ m, $t_{TX} = 49$ μ m, $s_{RX} = 100$ μ m, $s_{TX} = 165$ μ m, $n_{RX} = 2$, and $n_{TX} = 20$.

IV. INDUCTANCE, RESISTANCE, CAPACITANCE OF COIL

The accurate estimation of inductance and resistance for each iterative design is crucial because the PTE calculation heavily depends on those values. Each of these values must reflect the frequency dependency to allow the flexible use of this model while accurately modeling the impedance at different operating frequencies.

To calculate resistance, high-frequency effects such as skin effect and proximity effect are considered. Skin effect originates from current redistribution due to the changing magnetic field generated by the current in the conductor. Proximity effect resistance originates from the changing magnetic field generated by the nearby conductors. Therefore, the resistance due to skin effect and the resistance due to proximity effect are added to obtain the total resistance [23]:

$$R_{coil} = R_{skin} + R_{prox} \quad (1)$$

High-frequency AC currents suffer from skin effects in which electrons are crowded to the surface of the conductor in response

to the changing magnetic field [24], reducing the skin-depth. The skin-effect resistance is derived by Wheeler, where a conductor is modelled by treating it as a stack of thin slabs and the slabs are connected with internal inductances [25]. When the width and the height of the cross-section of the conductor is greater than twice the skin depth, the skin-effect resistance can be calculated by assuming that current flows only at the skin of the conductor. When either width or thickness is less than $2 \times$ skin depth, skin-effect resistance can be calculated from the profile of the current which decays exponentially with respect to the distance from the surface [26]. The skin-effect resistance is expressed as (2), where $\delta = \sqrt{\frac{\rho}{\pi\mu_0 f}}$ is the skin depth, ρ is the resistivity, f is the frequency, and R_{DC} is the DC resistance of the coil, w is the spiral width, and t is the planar thickness.

$$R_{\text{skin}} = \begin{cases} \frac{wt}{wt - (w - 2\delta)(t - 2\delta)} R_{DC} & \text{if } w, t > 2\delta \\ \frac{t}{\delta(1 - e^{-\frac{t}{\delta}})} R_{DC} & \text{else} \end{cases}$$

$$R_{DC} = R_{\text{sheet}} \frac{4n(OD - w) - 4(n - 1)n(s + w)}{w} \quad (2)$$

Proximity effect contributes to an increase in total resistance due to eddy currents induced by neighboring spiral turns. Eddy currents are induced from the changing magnetic field which is collectively generated by currents in neighboring sections of the coil. The eddy currents from proximity increase the effective resistance of the coil. The accuracy of the numerical calculation for proximity effect is improved by addressing the change of the magnetic field due to the eddy current [27]. The proximity-effect resistance is calculated and added for each turn.

$$R_{\text{prox}} = \begin{cases} \sum_{i=1}^n R_{\text{prox},i} & \text{if } t \frac{w^2}{w+s} > \frac{25\rho}{\mu_0} \\ 0 & \text{else} \end{cases} \quad (3)$$

Interestingly, the induced eddy currents also suffer from skin effect (Fig. 5b), where current flows at the edges of the conductor (teal and green), and not at the center (orange). If the conductor thickness is greater than the skin depth, it is important to incorporate skin effect when calculating the proximity effect (4).

$$R_{\text{prox},i} = \rho l_i \text{Real} \left[\gamma t \frac{(H(x_{\text{left},i}) - H(x_{\text{right},i}))^2}{I_{\text{coil}}^2} \coth \gamma w \right. \\ + 2\gamma t \frac{H(x_{\text{left},i})H(x_{\text{right},i})}{I_{\text{coil}}^2} \tanh \frac{\gamma w}{2} \\ - 2\frac{t}{w} \left(\frac{1}{2t} - \frac{H(x_{\text{left},i}) - H(x_{\text{right},i})}{I_{\text{coil}}} \right)^2 + \frac{1}{2wt} \\ \left. + 2\gamma \frac{t^2}{w} \left(\frac{1}{2t} - \frac{H(x_{\text{left},i}) - H(x_{\text{right},i})}{2I_{\text{coil}}} \right)^2 \cot h \frac{\gamma t}{2} \right] \quad (4)$$

Here, γ is complex propagation constant (defined as $\frac{1+j}{\delta}$), H is axial magnetic field, $x_{\text{left},i}$ is position of the left boundary of turn i (Fig 5a, red solid line), $x_{\text{right},i}$ is position of the right boundary of turn i (Fig 5a, red dotted line), and I_{coil} is the current through

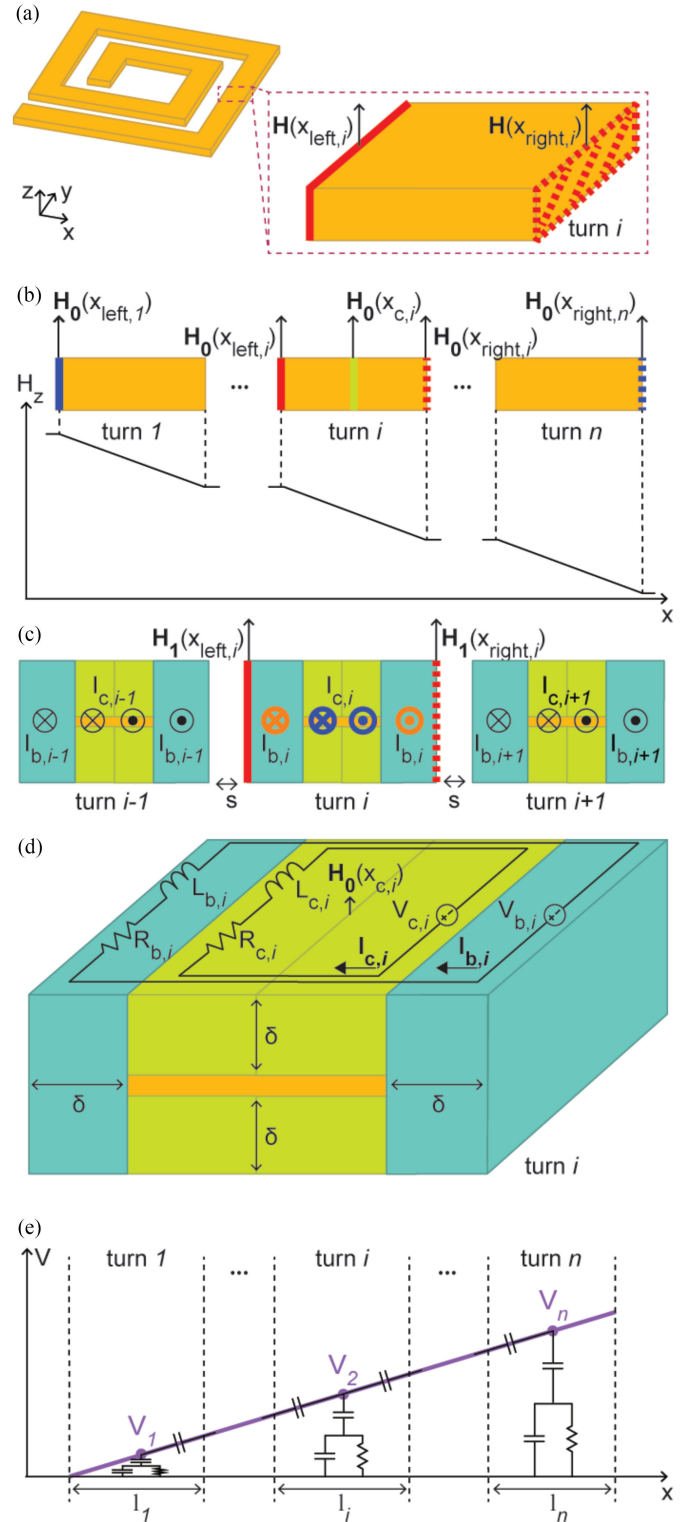


Fig. 5. a) z-component of the magnetic fields at left (red line) and right (red dotted line) boundary b) Nominal current-induced magnetic field at left boundary of turn 1 (blue line), left boundary (green line), center (green line), and right boundary of turn i (red dotted line), and right boundary of turn N (blue dotted line). c) Eddy current-induced magnetic field at left (red line) and right boundary of turn i (red dotted line). Eddy current in the side (tint) and the center (green) of each turn is modelled by line currents (orange and blue, respectively). d) Circuit model to obtain eddy currents in the side (tint) and center (green). e) Capacitive impedance model. Voltage of each turn is obtained at the mid-point of the turn (purple dot).

the coil [28]; and where the axial magnetic field is orthogonal to the plane of the spiral. The axial magnetic field (H) is a sum of the nominal current-induced magnetic field (H_0) and the eddy current-induced magnetic field (H_1).

$$H = H_0 + H_1 \quad (5)$$

The nominal current-induced magnetic field is calculated by linear approximation of the overall field distribution across the turns (67) [28].

$$H_0(x_{\text{left},1}) = \frac{n}{OD - ID} \ln \frac{\sqrt{OD^2 + t^2} + OD}{\sqrt{ID^2 + t^2} + ID} e^{\frac{ID}{OD}(0.4 + 0.15 \ln \frac{OD}{2t})}$$

$$H_0(x_{\text{right},n}) = \frac{n(0.1 + 0.08 \ln \frac{OD}{2t})}{OD - ID} \ln \frac{\sqrt{OD^2 + t^2} + OD}{\sqrt{ID^2 + t^2} + ID} e^{\frac{ID}{OD}(1 + \frac{1}{8} \ln \frac{OD}{2t})} \quad (6)$$

$$H_0(x_{\text{left},i}) = \frac{n-i+1}{n} H_0(x_{\text{left},1}) + \frac{i-1}{n} H_0(x_{\text{right},n})$$

$$H_0(x_{\text{right},i}) = \frac{n-i}{n} H_0(x_{\text{left},1}) + \frac{i}{n} H_0(x_{\text{right},n})$$

$$H_0(x_{\text{right},i}) = \frac{n-i+0.5}{n} H_0(x_{\text{left},1}) + \frac{i-0.5}{n} H_0(x_{\text{right},n}) \quad (7)$$

The expressions for the nominal current-induced magnetic field at the left boundary of turn 1 ($H_0(x_{\text{left},1})$, blue line in Fig. 5b) and right boundary of turn n ($H_0(x_{\text{right},n})$, blue dotted line in Fig. 5b) (6) are obtained from data-fitting [28]. The nominal current-induced magnetic field at the left boundary of turn i ($H_0(x_{\text{left},i})$, red line in Fig. 5b), right boundary of turn i ($H_0(x_{\text{right},i})$, red dotted line in Fig. 5b), and center of turn i ($H_0(x_{c,i})$, green circle in Fig. 5b) are expressed as the fractions of (7).

Eddy currents are modeled as two separate current paths at each turn (Fig. 5c, teal and green). The current path in the left and right (Fig. 5c, teal) are modeled as two line currents having opposite direction ($I_{b,i}$, orange in Fig. 5c). The current path in the top and bottom (Fig. 5c, green) is also modeled as two line currents having opposite direction ($I_{c,i}$, blue in Fig. 5c). The eddy current-induced magnetic field at the left side of turn i ($H_1(x_{\text{left},i})$, red circle in Fig. 5c) and right side of turn i ($H_1(x_{\text{right},i})$, red dotted circle in Fig. 5c) are obtained by adding the contribution of eddy currents (8, 9), where s is the turn spacing and w is the spiral width.

$$H_1(x_{\text{left},i}) = \frac{1}{2\pi} \left(-\frac{I_{b,i-1}}{s+w-0.5\delta} - \frac{I_{c,i-1}}{s+0.75w-0.5\delta} + \frac{I_{b,i-1}}{s+0.5\delta} + \frac{I_{c,i-1}}{s+0.25w+0.5\delta} + \frac{I_{c,i}}{0.25w+0.5\delta} - \frac{I_{c,i}}{0.75w-0.5\delta} - \frac{I_{b,i}}{w-0.5\delta} \right) + \frac{I_{b,i}}{2\delta+2t} \quad (8)$$

$$H_1(x_{\text{right},i}) = \frac{1}{2\pi} \left(-\frac{I_{b,i}}{w-0.5\delta} - \frac{I_{c,i}}{0.75w-0.5\delta} \right)$$

$$- \frac{I_{c,i}}{0.25w+0.5\delta} + \frac{I_{b,i+1}}{s+0.5\delta} + \frac{I_{c,i+1}}{s+0.25w+0.5\delta} - \frac{I_{c,i+1}}{s+0.75w-0.5\delta} - \frac{I_{b,i+1}}{s+w-0.5\delta} \Big) + \frac{I_{b,i}}{2\delta+2t} \quad (9)$$

To obtain expressions for $I_{b,i}$ and $I_{c,i}$, a circuit model consisting of resistances, inductances, and voltage sources is adapted from a typical proximity effect model in 2-dimensions [27]. By solving the circuit as a two-port network, $I_{b,i}$ and $I_{c,i}$ are expressed using current sources (10). Here, the voltage sources (Fig. 5d, $V_{b,i}$ and $V_{c,i}$) represent the electromotive force caused by the nominal current-induced magnetic field. $V_{b,i}$ and $V_{c,i}$ are obtained using Faraday's law, where $H_{c,i}$ is the average magnetic field enclosed by the eddy circuits of turn i . The ohmic power dissipation from the eddy currents is modeled using resistors (Fig. 5d, $R_{b,i}$ and $R_{c,i}$). The length of the current path is set to $2 \times$ length of each turn to account for the bidirectional eddy current. The thickness is identical to the skin depth. The resistances are calculated by using the length of the current path and the thickness of the current path. The expressions for $L_{b,i}$ and $L_{c,i}$ are based on a self-inductance model for square spiral coil [29]. The mutual inductance (Fig. 5d, $M_{b-c,i}$) represents the coupling between $L_{b,i}$ and $L_{c,i}$ [29].

$$\begin{bmatrix} I_{b,i} \\ I_{c,i} \end{bmatrix} = \frac{\begin{bmatrix} j\omega\mu_0 H_{c,i} l_i (w-\delta) \\ j\omega\mu_0 H_{c,i} l_i (0.5w-\delta) \end{bmatrix}}{\begin{bmatrix} \frac{2\rho l_i}{\delta t} + \frac{j\omega\mu_0 l_i}{\pi} \ln \frac{2(w-\delta)}{\delta+t} & j\omega M_{b-c,i} \\ j\omega M_{b-c,i} & \frac{2\rho l_i}{\delta(0.5w-\delta)} + \frac{j\omega\mu_0 l_i}{\pi} \ln \frac{2w-4\delta}{0.5w+\delta} \end{bmatrix}} \quad (10)$$

Once the proximity resistance is calculated, inductance is obtained as (11) [21], [22] where μ_0 is vacuum permeability, $\phi = \frac{OD-ID}{OD+ID}$ is fill ratio, $M_{b\text{-coil},i}$ is mutual inductance between $L_{b,i}$ and the coil, and $M_{c\text{-coil},i}$ is mutual inductance between $L_{c,i}$ and the coil.

$$L_{\text{coil}} = 2.34\mu_0 n^2 \frac{OD+ID}{2} \frac{1}{1+2.75\phi} - \sum_{i=1}^n M_{b\text{-coil},i} I_{b,i} - \sum_{i=1}^n M_{c\text{-coil},i} I_{c,i} \quad (11)$$

Lastly, the capacitance network of the coil is estimated. Considering an IC manufacturing process and the use of silicon as a base substrate for an RX coil, the network can be built by adding the parasitic capacitance between adjacent turns (C_{coil}), oxide capacitance (C_{ox}), total silicon capacitance (C_{si}), and silicon resistance (R_{si}) [30]. In regard to a PCB manufacturing process for a TX coil, substrate leakage is neglected. C_{coil} is obtained from the summation of the capacitance between turn i and turn

$i+1$ (12), adjusted by coefficients [31], [32].

$$C_{\text{coil}} = \sum_{i=1}^{n-1} \left(\frac{0.5(l_i + l_{i+1})}{l_{\text{tot}}} \right)^2 \left(\epsilon_{\text{ins}} \frac{0.5(l_i + l_{i+1})t}{s} + C_{\text{fr},i} \right) \quad (12)$$

$$C_{\text{fr},i} = \frac{0.5(l_i + l_{i+1}) \epsilon_{\text{ins}} \frac{\pi}{r} K \left(\frac{r^2-1}{r^2} \right)}{\frac{1}{r+1} \left[3.93K \left(\frac{(r-1)^2}{(r+1)^2} \right) - \pi F_3 \left(0.50.51, \frac{(r-1)^2}{(r+1)^2} \right) - \pi F_2 \left(0.50.51, \frac{(r-1)^2}{(r+1)^2} \right) + \ln \left(\frac{r+1}{r-1} \right) \frac{1}{r} K \left(\frac{r^2-1}{r^2} \right) \right]} \quad (13)$$

To simplify the equation, the voltage of each turn is assumed to be constant and proportional to the length from the start of the coil to the midpoint of the turn (Fig. 5e). Capacitance between turn i and $i+1$ is the combination of fringe capacitance ($C_{\text{fr},i}$) and parallel plate capacitance (12), where ϵ_{ins} is effective permittivity of the space between the turns [10]. $C_{\text{fr},i}$ is obtained from the electrostatic capacitance of coplanar strips [33] (13), where $r = \frac{s+2w}{s}$, K is complete elliptic function of the first kind, and F_j is the derivative of the Gaussian hypergeometric function with respect to the j th variable. C_{ox} , C_{si} , and R_{si} are obtained from the summation of the oxide capacitance, substrate capacitance, and substrate conductance of turn i , respectively (14), where ϵ_{ox} is the permittivity of the insulator between the metal and the substrate, t_{ox} is the thickness of the insulator between the metal and the substrate, C_{sub} is the capacitance of the substrate in unit area, and G_{sub} is the conductance of the substrate in unit area.

$$\begin{aligned} C_{\text{ox}} &= \sum_{i=1}^n \left(\frac{0.5l_i + \sum_{j=1}^{i-1} l_j}{l_{\text{tot}}} \right)^2 w l_i \frac{\epsilon_{\text{ox}}}{t_{\text{ox}}} \\ C_{\text{si}} &= \sum_{i=1}^n \left(\frac{0.5l_i + \sum_{j=1}^{i-1} l_j}{l_{\text{tot}}} \right)^2 w l_i C_{\text{sub}} \\ \frac{1}{R_{\text{si}}} &= \sum_{i=1}^n \left(\frac{0.5l_i + \sum_{j=1}^{i-1} l_j}{l_{\text{tot}}} \right)^2 w l_i G_{\text{sub}} \end{aligned} \quad (14)$$

At this point, the self-resonant frequency for this coil without resistance can be acquired by using R_{coil} , L_{coil} and C_{coil} . In order to shift the resonant frequency to the operation frequency, tuning capacitor values for each coil can be calculated by considering parasitic capacitance values.

$$f_{\text{self}} = \frac{1}{2\pi} \sqrt{\frac{1}{L_{\text{coil}} C_{\text{coil}}} - \frac{R_{\text{coil}}}{L_{\text{coil}}}} \quad (15)$$

V. VALIDATION STUDY

The design algorithm implements the design process presented in previous sections and yields design parameters for the set of coils, along with an estimate of the PTE. The accuracy of the estimates is validated by comparing the PTE obtained from the presented method for a set of design parameters to the PTE measured from an FEM constructed about the same set of

parameters. Focus is placed upon the set of design parameters which are relevant to associated work in contemporary biomedical device applications; the accuracy of the estimated PTE about each of the key design parameters is explored only about the realm of interest (Fig 6). To quantitatively measure the validity of the proposed method, accuracies are calculated by subtracting the difference between PTE of the proposed model and the FEM from 100 PTE% (16).

$$\text{Accuracy} = (100 - \Delta) \text{ PTE\%} \quad (16)$$

$$\Delta = |\text{PTE}_{\text{Model}} - \text{PTE}_{\text{FEM}}| \quad (17)$$

When OD_{RX} is varied from 1–15 mm, the average accuracy is 99.5 PTE% and the standard deviation is 1% for the entire range (Fig. 6a). The average accuracy in PTE for OD_{TX} between 1–50 mm is 97 PTE% and the deviation is 2% (Fig. 6b).

ID_{RX} within 1–14.5 mm shows the PTE accuracy of 93 PTE% with the deviation of 5 PTE% (Fig. 6c). The peak accuracy is measured at around ID_{RX} of 13 mm but then decreases at higher ID_{RX} . A decreasing distance between OD and ID forces the turn width and turn spacing to be narrower, therefore creating higher resistance. For values of ID_{RX} beyond 13mm, PTE is underestimated because the proximity resistance of RX coil is overestimated. The mismatch in the proximity resistance is due to the overestimation of the magnetic field generated by neighboring currents. The same observation can be applied to ID_{TX} (Fig. 6d).

When ID_{TX} is between 1–48 mm, the mean accuracy is 94 PTE% and the deviation is 7% (Fig. 6d). The maximum PTE is achieved when ID_{TX} is around 20 mm. This is mainly due to the relatively high k at the ID/OD ratio of 0.4 (blue in Fig. 3f).

For t_{RX} between 1–30 μm , the mean accuracy is 98 PTE% with std. deviation of 2 PTE% (Fig. 6e). For t_{TX} of 5–500 μm , the mean accuracy is 96 PTE% where standard deviation is 5 PTE%. In general, the thicker the coil is, the higher PTE it can achieve [33] (Fig. 6f). However, the effect is marginal. The relatively low rate of increase of PTE with respect to the planar thickness is because most of the additional cross-sectional conducting area is not utilized due to the skin effect [34].

RX coils with the width of 0.01–7 mm show the average accuracy of 92 PTE% with standard deviation of 7 PTE% (Fig. 6g). The efficiency is overestimated for $w_{\text{RX}} > 3$ mm. For these coils, inductances are also overestimated (>50%). w_{TX} between 1–20 mm corresponds to an average accuracy of 94 PTE% with standard deviation of 4 PTE% (Fig. 6h). Notably, PTE is essentially constant over the explored range of w_{TX} .

n_{RX} between 1–15 corresponds to PTE prediction accuracy of 92 PTE% with standard deviation of 15 PTE% (Fig. 6i). Average accuracy is 98 PTE% and standard deviation of accuracy is 2 PTE% when n_{TX} is between 1–15 (Fig. 6j). Interestingly, PTE is constant over the explored range of n_{TX} . s_{RX} between 0.01–1 mm shows average accuracy of 95 PTE% with standard deviation of 4 PTE% (Fig. 6k). For s_{TX} within the range of 0.11–5 mm, PTE prediction shows average accuracy of 97 PTE% with standard deviation of 2 PTE% (Fig. 6l). Overall, average

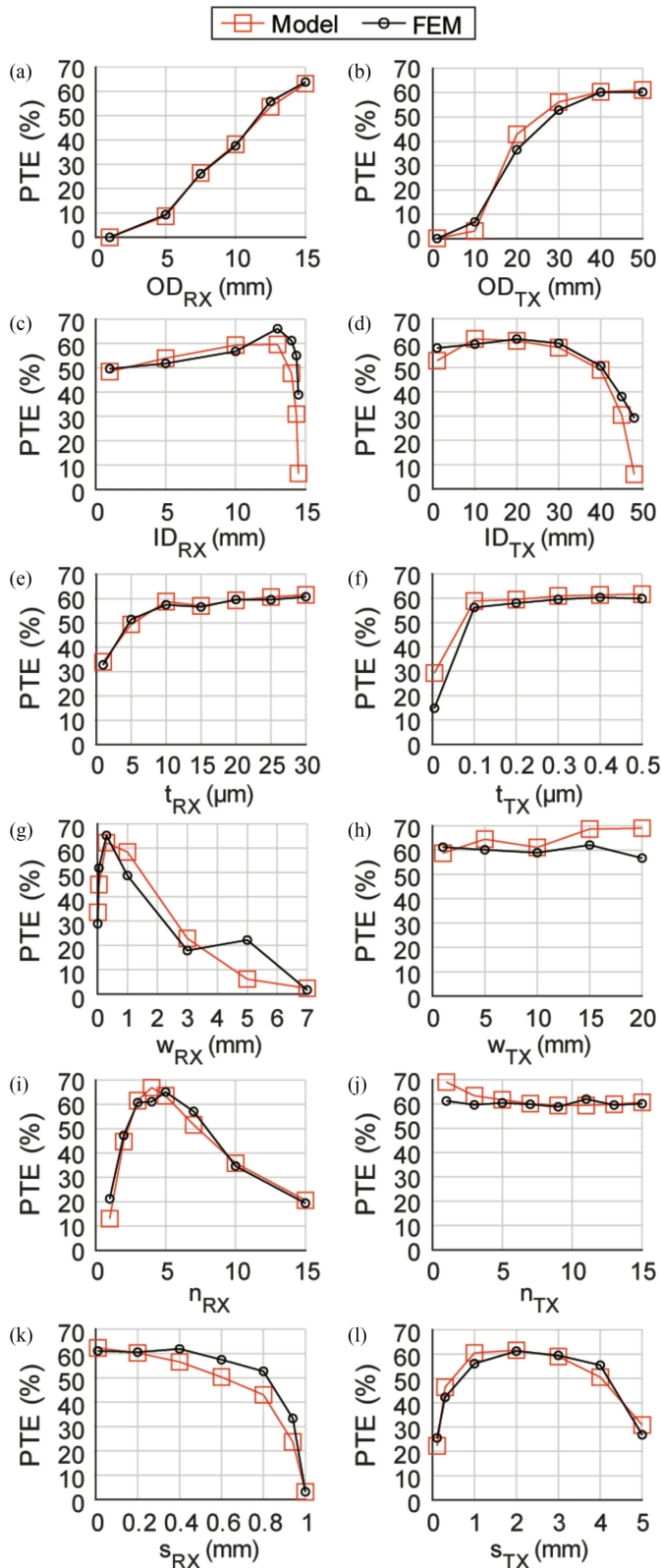


Fig. 6. Power transfer efficiency as a function of geometrical parameters where (red) squares are the design algorithm predictions, and (black) circles are the source FEM used for validation; outer diameter of the RX coil, b) outer diameter of the TX coil, c) inner diameter of the RX coil, d) inner diameter of the TX coil, e) thickness of the RX coil, f) thickness of the TX coil, g) width of the RX coil, h) width of the TX coil, i) turn count of the RX coil, j) turn count of the TX coil, k) spacing of the coil, and l) spacing of the TX coil.

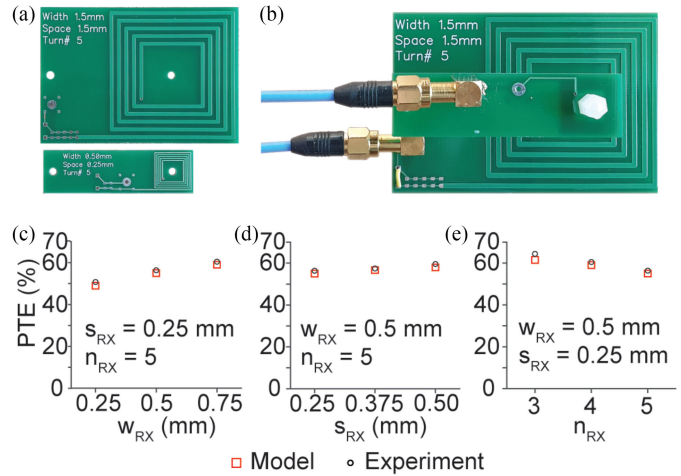


Fig. 7. Validation study using fabricated coils. a) Receiver and transmitter coils are fabricated on PCBs. b) Test setup to measure the coupling between the two coils. c-e) The extracted PTE with varying w_{RX} , s_{RX} , and n_{RX} are plotted and compared to the PTE calculated from the proposed model.

accuracy of PTE estimation is 95 PTE% with standard deviation of 6 PTE%.

The design process yields coil pairs with an estimated PTE which closely match the PTE obtained from a corresponding FEM. The observation applies for each of the key design parameters, such as the inner diameter, outer diameter, thickness, width, the number of turns, and spacing for both RX and TX coils (Fig. 6a-l). Exceptions occur where there are large ID_{RX} (Fig. 6b) and small numbers of turns (Fig. 6g-j) where the mismatch becomes significant. Also, the proposed method performs poorly when using high frequency over 30 MHz due to the secondary effect affecting boundary conditions while calculating the proximity effect and analytic calculation deviates from FEM result [28]. The optimal boundary to achieve high accuracy using this proposed model is below 30 MHz. Also, the turn count should be larger than 2 and the overall size of coils should be less than 10 cm.

The design algorithm is validated using fabricated planar coils (Fig. 7). The planar coils for the transmitter and receivers are fabricated using a 2-layer standard PCB manufacturing. In order to test the accuracy of the algorithm with varying width, spacing, and turn counts, 7 different designs of receiver coils are designed and fabricated. The tested widths are 0.25 mm, 0.5 mm, and 0.75 mm; the tested spacings are 0.25 mm, 0.375 mm, and 0.5 mm; and the tested turn counts are 3, 4, and 5. For every measurement, the receiver and transmitter coils are spaced to 15 mm using a plastic screw (Fig. 7b). The transmitter coil is design with a width of 1.5 mm, spacing of 1.5 mm, and turn count of 5. For this test, we used 13.56 MHz. The set of s-parameters is measured using a network analyzer (Keysight Technologies PNA-L N5234A). The measured s-parameters are then converted to z-parameters before extracting the PTE between the two coils. The experimental PTEs agrees well with the model PTEs in every tested parameter (95.5% to 98.8%).

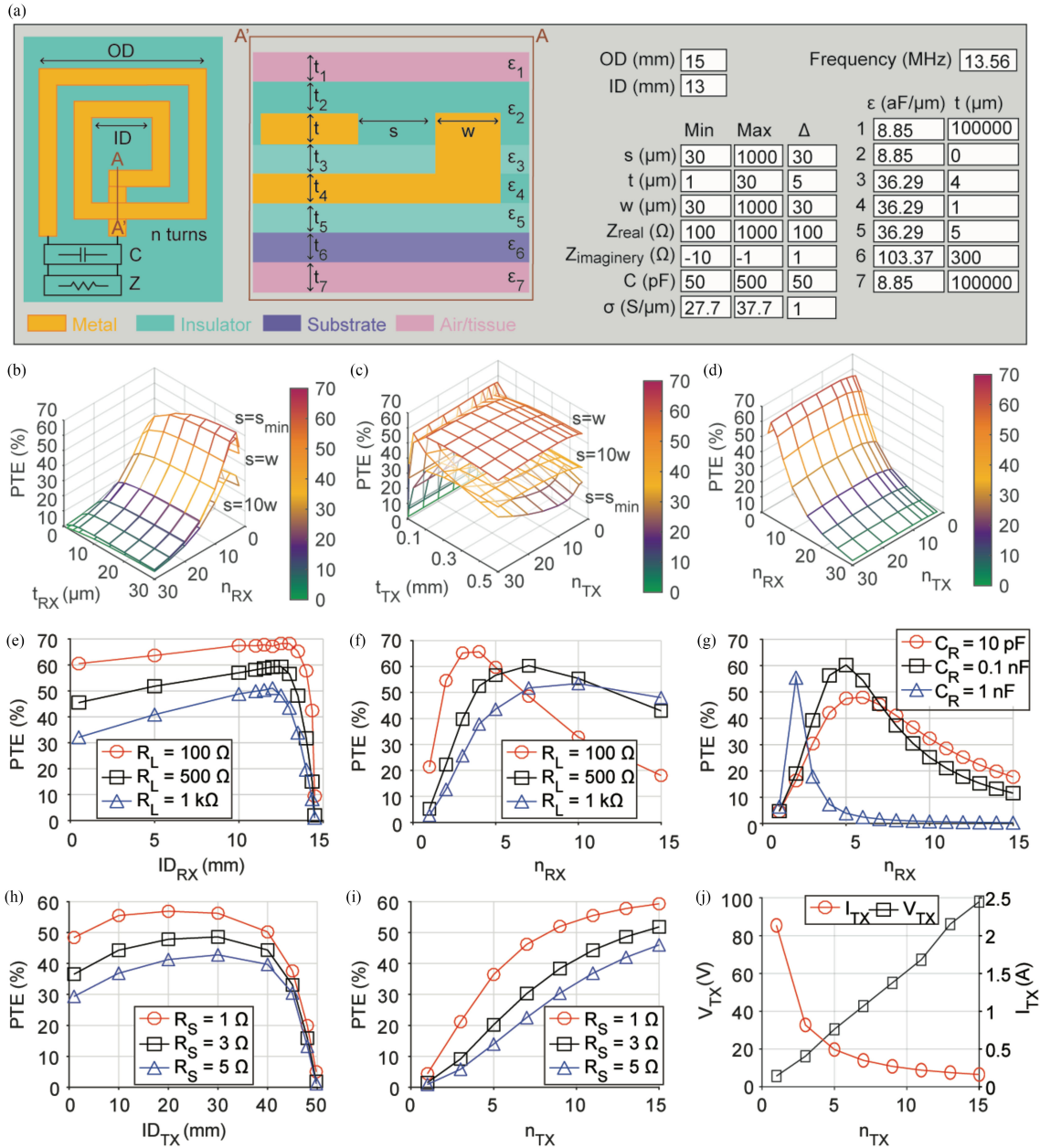


Fig. 8. User interface of the design automation software. a) GUI allows user to put ODs and IDs chosen from the k-chart, manufacturing constraints, and circuit components attached to the coils into the software. The graphical output of the software includes (b) power efficiency versus inner diameter and thickness of TX coil, (c) power efficiency versus inner diameter and thickness of RX coil, (d) power efficiency versus thickness and turn count of TX coil when the width is same as the thickness, (e) power efficiency versus inner diameter of RX coil and load resistance, (f) power efficiency versus turn count of RX coil and load resistance, (g) power efficiency versus tuning capacitance and turn count of RX coil, (h) power efficiency versus inner diameter of TX coil and source resistance, (i) power efficiency versus turn count of TX coil and source resistance, and (j) voltage across the TX coil (black square) and current through the TX coil (red circle) versus turn count of TX and RX coil.

VI. DESIGN AUTOMATION SOFTWARE

The design automation software is intended to be an open-source MATLAB application. A minimalist approach is taken, where the application is designed for immediate use and generality. To use the application, the user must first input the desired ID, OD, d for their application. The interface then prompts the user to input their constraining fabrication capabilities (Fig 8a). The manufacturing capability is an important input to this software for it to accurately estimate the optimal PTE. The parameters

include the minimum, maximum, and incremental value of width, spacing, and thickness of the planar square-spirals, and the physical properties of the conductive and insulation layers (resistivity and permittivity). It is assumed that the user shall have a previous knowledge of the constraints imposed by their device application or the accessible manufacturing process. It is also assumed that the manufacturing process conforms to the planar square spiral geometry, such as for a PCB or IC.

Once the requisite input data has been given, the application executes the design flow discussed in previous sections. The

application computes PTE from combinations of the design parameters (Fig. 8b–d). The software outputs the set of design parameters that will achieve the maximum power transfer efficiency based on the given constraints.

First, a virtual reference RX coil is generated based on median design parameters within range of the user’s inputs. PTE is then calculated for combinations of virtual TX coils (Fig. 8b) with respect to the reference RX coil. From the combination of TX coils, those parameters which achieve the maximum PTE are obtained. Next, the selected parameters for the TX coil are used as reference to obtain the best set of RX parameters (Fig. 8c) from PTE calculations against combinations of virtual RX coils.

Although the best set of parameters based on a constraint is obtained from the software, the constraint is often practically a range instead of a single value. The software provides the best set of parameters according to the user’s design philosophy. For example, load resistance of RX coil depends on the power consumption of the implant circuit. The ideal design parameter values for the best coil pair are thus affected by the load. Regarding the effective series resistance from ID_{RX} , PTE peaks at 13 mm when the load is 100 Ω and PTE peaks at 12 mm when the load is 1 k Ω (Fig. 8e).

Here, the choice of ID_{RX} is up to the design objective of the user. One design philosophy may be to maximize the efficiency for a severe power demanding mode because it determines the maximum power of the transmitter. In this case, 13 mm is chosen as ID_{RX} . Another design philosophy is to maximize the efficiency for both severe and mild power demanding mode; where the value of load in practice is uncertain, so there must be a tolerance for a range of PTE. The average PTE is higher for ID_{RX} of 12 mm (59%) than for ID_{RX} of 13 mm (56%), thus ID_{RX} should be 12 mm. There are other design philosophies, such as those which may value increasing ID_{RX} to secure more area for the implant circuit.

Naturally, the optimal n_{RX} is also affected by the load resistance (Fig. 8f). In the design example, if the user chooses to maximize PTE for the heaviest load (100 Ω), the optimal turn count will be 3. If user chooses to maximize PTE for both 100 Ω and 500 Ω load resistances, the optimal turn count will be 5. If user chooses to maximize PTE for the load resistance of 500 Ω and 1 k Ω , the optimal turn count will be 10. In addition to the load resistance, parameters of the RX coil are also affected by the resonant capacitance defined by the operating frequency. The RX parameter that depends on the resonant capacitance most is the number of turns. In our example, the optimum turn count of RX coil is 5 when the available resonant capacitance is less than 200 pF and the optimum turn count is 3 otherwise (Fig 8g).

Constraints that affect TX coil is the source resistance representing ohmic loss of the TX circuitry and the maximum allowed voltage of the TX coil. The source resistance alters optimum ID_{TX} (Fig 8h). From the design example, the optimum inner diameter also is 30 mm when the source resistance is 3 Ω or 5 Ω and it is 20 mm when the source resistance is 1 Ω . The source resistance also significantly affects the number of turns (Fig 8i) in the TX coil. PTE decreases as the source resistance increases; there is a notable loss to PTE where n_{TX} (average PTE loss > 0.3 for n_{TX} <5) is low and mild loss where n_{TX} is

high (average PTE loss < 0.2 for n_{TX} > 10). The effect of the source resistance makes the high number of turn favorable for best PTE. On the other hand, high turn counts of TX coil are associated with the high voltage across TX coil (Fig 8j), which is not desirable considering that TX coil is attached to the skin of the recipient. If the maximum allowed voltage of TX coil is set as 20 V, optimum n_{TX} is 3, which corresponds to PTE of 0.2 for the source resistance of 1 Ω . To achieve higher PTE with the same maximum allowed voltage, modification of the coil structure such as segmenting [36] should be considered.

There are other constraints which are important but not explored in this paper, i.e., effect of tissue, misalignment, curvature of the coils, distance variation, specific absorption rate, power loss of rectifier, and substrate loss variation. It may also be possible to optimize the search process to navigate through the combination of parameters with guidance so that the amount of computation for this process is minimized. However, this paper serves as a practical steppingstone towards those future works.

The MATLAB code for the design automation may be found in the lab repository at:

<https://github.com/bioelectronicsUCF/CoilDesign>.

VII. CONCLUSION

A design automation method for wireless power coils is proposed and implemented with the objective of maximizing power transfer efficiency. The power transfer efficiency depends mostly upon the inductive coupling coefficient, k , of a set of coils. Computational complexity can be reduced by isolating the k from other design parameters and iterating coil designs about the remaining practical range of freedom. An analytic circuit model is derived to calculate and identify the maximum PTE from the set of the design parameters for each coil pair. The equivalent analytic model includes novel formulations for the proximity effect, skin effect and parasitic losses. The model is validated with respect to all design parameters using FEM. An open-source design automation software is developed based on the analytic model to yield the optimal design parameters for maximum PTE on a typical contemporary desktop computer. The automation software is freely accessible to lower the barriers of development for wireless neuro-prosthetic devices and sensors in the hope that the community continues to thrive.

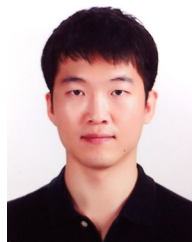
ACKNOWLEDGMENT

The authors would like to thank UCF Advanced Research Computing Center for providing computational resources.

REFERENCES

- [1] K. Agarwal, R. Jegadeesan, Y. Guo, and N. V. Thakor, “Wireless power transfer strategies for implantable bioelectronics,” *IEEE Rev. Biomed. Eng.*, vol. 10, pp. 136–161, 2017.
- [2] A. K. RamRakhyani, S. Mirabbasi, and M. Chiao, “Design and optimization of resonance-based efficient wireless power delivery systems for biomedical implants,” *IEEE Trans. Biomed. Circuits Syst.*, vol. 5, no. 1, pp. 48–63, Feb. 2010.
- [3] A. Ma and A. S. Y. Poon, “Midfield wireless power transfer for bioelectronics,” *IEEE Trans. Circuits Syst. Magn.*, vol. 15, no. 2, pp. 54–60, Apr.–Jun. 2015.

- [4] A. Abid *et al.*, "Wireless power transfer to millimeter-sized gastrointestinal electronics validated in a swine model," *Sci. Rep.*, vol. 7, no. 1, Apr. 2017, Art. no. 46745.
- [5] A. Ibrahim and M. Kiani, "A figure-of-merit for design and optimization of inductive power transmission links for millimeter-sized biomedical implants," *IEEE Trans. Biomed. Circuits Syst.*, vol. 10, no. 6, pp. 1100–1111, Dec. 2016.
- [6] D. Ahn and M. Ghovanloo, "Optimal design of wireless power transmission links for millimeter-sized biomedical implants," *IEEE Trans. Biomed. Circuits Syst.*, vol. 10, no. 1, pp. 125–137, Feb. 2016.
- [7] M. Zargham and P. G. Gulak, "Fully integrated on-chip coil in 0.13 μm CMOS for wireless power transfer through biological media," *IEEE Trans. Biomed. Circuits Syst.*, vol. 9, no. 2, pp. 259–271, Apr. 2015.
- [8] K. Van Schuylenbergh and R. Puers, *Inductive Powering: Basic theory and Application to Biomedical Systems*. Berlin, Germany: Springer Science & Business Media, 2009.
- [9] R. A. Harrison, "Designing efficient inductive power links for implantable devices," in *Proc. IEEE Int. Symp. Circuits Syst.*, 2007, pp. 2080–2083.
- [10] U. Jow and M. Ghovanloo, "Modeling and optimization of printed spiral coils in air, saline, and muscle tissue environments," *IEEE Trans. Biomed. Circuits Syst.*, vol. 3, no. 5, pp. 339–347, Oct. 2009.
- [11] A. Kurs, A. Karalis, R. Moffatt, J. D. Joannopoulos, P. Fisher, and M. Soljačić, "Wireless power transfer via strongly coupled magnetic resonances," *Science*, vol. 317, no. 5834, pp. 83–86, 2007.
- [12] A. A. Eteng, S. K. Abdul Rahim, C. Y. Leow, B. W. Chew, and G. A. Vandenbosch, "Two-stage design method for enhanced inductive energy transmission with Q-constrained planar square loops," *Plos One*, vol. 11, no. 2, p. e0148808. [Online]. Available: <https://doi.org/10.1371/journal.pone.0148808>
- [13] Z. Duan, Y.-X. Guo, and D.-L. Kwong, "Rectangular coils optimization for wireless power transmission," *Radio Sci.*, vol. 47, no. 03, pp. 1–10, 2012.
- [14] P. Feng, P. Yeon, Y. Cheng, M. Ghovanloo, and T. G. Constandinou, "Chip-scale coils for millimeter-sized bio-implants," *IEEE Trans. Biomed. Circuits Syst.*, vol. 12, no. 5, pp. 1088–1099, Oct. 2018.
- [15] Y. Cheng, G. Wang, and M. Ghovanloo, "Analytical modeling and optimization of small solenoid coils for millimeter-sized biomedical implants," *IEEE Trans. Microw. Theory Tech.*, vol. 65, no. 3, pp. 1024–1035, Mar. 2017.
- [16] S. A. Mirbozorgi, P. Yeon, and M. Ghovanloo, "Robust wireless power transmission to mm-sized free-floating distributed implants," *IEEE Trans. Biomed. Circuits Syst.*, vol. 11, no. 3, pp. 692–702, Jun. 2017.
- [17] S. Kim, J. S. Ho, and A. S. Poon, "Wireless power transfer to miniature implants: Transmitter optimization," *IEEE Trans. Antennas Propag.*, vol. 60, no. 10, pp. 4838–4845, Oct. 2012.
- [18] M. Dannhauer, B. Lanfer, C. H. Wolters, and T. R. Knösche, "Modeling of the human skull in EEG source analysis," *Hum. Brain Mapping*, vol. 32, no. 9, pp. 1383–1399, 2011.
- [19] D. De Kegeel, J. Vastmans, H. Fehervary, B. Depreitere, J. Vander Sloten, and N. Famaey, "Biomechanical characterization of human dura mater," *J. Mech. Behav. Biomed. Mater.*, vol. 79, pp. 122–134, Mar. 2018.
- [20] K. Chopra *et al.*, "A comprehensive examination of topographic thickness of skin in the human face," *Aesthetic Surg. J.*, vol. 35, no. 8, pp. 1007–1013, 2015.
- [21] H. A. Wheeler, "Simple inductance formulas for radio coils," *Proc. Inst. Radio Eng.*, vol. 16, no. 10, pp. 1398–1400, 1928.
- [22] S. S. Mohan, M. del Mar Hershenson, S. P. Boyd, and T. H. Lee, "Simple accurate expressions for planar spiral inductances," *IEEE J. Solid-State Circuits*, vol. 34, no. 10, pp. 1419–1424, Oct. 1999.
- [23] J. A. Ferreira, "Improved analytical modeling of conductive losses in magnetic components," *IEEE Trans. Power Electron.*, vol. 9, no. 1, pp. 127–131, Jan. 1994.
- [24] H. A. Haus and J. R. Melcher, *Electromagnetic Fields and Energy*. Upper Saddle River, NJ, USA: Prentice Hall Englewood Cliffs, 1989.
- [25] H. A. Wheeler, "Formulas for the skin effect," *Proc. IRE*, vol. 30, no. 9, pp. 412–424, 1942.
- [26] U.-M. Jow and M. Ghovanloo, "Design and optimization of printed spiral coils for efficient transcutaneous inductive power transmission," *IEEE Trans. Biomed. Circuits Syst.*, vol. 1, no. 3, pp. 193–202, Sep. 2007.
- [27] W. B. Kuhn and N. M. Ibrahim, "Analysis of current crowding effects in multiturn spiral inductors," *IEEE Trans. Microw. Theory Tech.*, vol. 49, no. 1, pp. 31–38, Jun. 2001.
- [28] X. Fang, R. Wu, and J. K. Sin, "Analytical modeling of AC resistance in thick coil integrated spiral inductors," *IEEE Trans. Electron Devices*, vol. 63, no. 2, pp. 760–766, Feb. 2016.
- [29] S. Jenei, B. K. Nauwelaers, and S. Decoutere, "Physics-based closed-form inductance expression for compact modeling of integrated spiral inductors," *IEEE J. Solid-State Circuits*, vol. 37, no. 1, pp. 77–80, Jan. 2002.
- [30] C. P. Yue and S. S. Wong, "Physical modeling of spiral inductors on silicon," *IEEE Trans. Electron Devices*, vol. 47, no. 3, pp. 560–568, Mar. 2000.
- [31] C.-H. Wu, C.-C. Tang, and S.-I. Liu, "Analysis of on-chip spiral inductors using the distributed capacitance model," *IEEE J. Solid-State Circuits*, vol. 38, no. 6, pp. 1040–1044, Jun. 2003.
- [32] A. Zolfaghari, A. Chan, and B. Razavi, "Stacked inductors and transformers in CMOS technology," *IEEE J. Solid-State Circuits*, vol. 36, no. 4, pp. 620–628, Apr. 2001.
- [33] F. R. Zypman, "Mathematical expression for the capacitance of coplanar strips," *J. Electrostat.*, vol. 101, 2019, Art. no. 103371.
- [34] R. Wu, S. Raju, M. Chan, J. K. O. Sin, and C. P. Yue, "Silicon-embedded receiving coil for high-efficiency wireless power transfer to implantable biomedical ICs," *IEEE Electron Device Lett.*, vol. 34, no. 1, pp. 9–11, Jan. 2013.
- [35] K. Chen and Z. Zhao, "Analysis of the double-layer printed spiral coil for wireless power transfer," *IEEE J. Emerg. Sel. Top. Power Electron.*, vol. 1, no. 2, pp. 114–121, Jun. 2013.
- [36] S. Stoecklin, A. Yousaf, G. Gidion, and L. Reindl, "Efficient wireless power transfer with capacitively segmented RF coils," *IEEE Access*, vol. 8, pp. 24397–24415, 2020.



Chaebin Kim (Member, IEEE) received the B.S. and Ph.D. degrees in electrical and computer engineering from Seoul National University, Seoul, South Korea, in 2014 and 2019, respectively. He is currently a Postdoctoral Fellow with Brain Science Institute, the Korea Institute of Science and Technology, Seoul, South Korea. From 2019 to 2020, he was Postdoctoral Fellow with Dr. Brian N. Kim's research lab, the University of Central Florida, Orlando, FL, USA.



Brian N. Kim (Member, IEEE) received the B.S. degree (with distinction) in electronics and computer engineering from Hanyang University, Seoul, South Korea, in 2008 and the Ph.D. degree in biophysics from Cornell University, Ithaca, NY, USA, in 2013. He is currently an Assistant Professor of electrical and computer engineering with the University of Central Florida, Orlando, FL, USA. From 2014 to 2015, he was Senior Electrical Engineer with Stratos Genomics Inc., Seattle, WA, USA. From 2013 to 2014, he was Postdoctoral Fellow in bioengineering with the University of California, Berkeley, CA, USA. His research interests include single-cell electrophysiology, brain-machine interface, and medical diagnostics.